ARTICLES

Journal of Semiconductors
(2020) 41, 052206
doi: 10.1088/1674-4926/41/5/052206

Two-dimensional transition metal dichalcogenides for lead halide perovskites-based photodetectors: band alignment investigation for the case of $CsPbBr_3/MoSe_2$

Le Huang[1], Nengjie Huo[2], Zhaoqiang Zheng[1], Huafeng Dong[3, †], and Jingbo Li[1, 2, 4, †]

[1]School of Materials and Energy, Guangdong University of Technology, Guangzhou 510006, China

[2]Institute of Semiconductor Science and Technology, South China Normal University, Guangzhou 510631, China

[3]School of Physics and Optoelectronic Engineering, Guangdong University of Technology, Guangzhou 510006, China

[4]State Key Laboratory of Superlattices and Microstructures, Institute of Semiconductors, Chinese Academy of Sciences, Beijing 100083, China

Abstract: The distinguished electronic and optical properties of lead halide perovskites (LHPs) make them good candidates for active layer in optoelectronic devices. Integrating LHPs and two-dimensional (2D) transition metal dichalcogenides (TMDs) provides opportunities for achieving increased performance in heterostructured LHPs/TMDs based optoelectronic devices. The electronic structures of LHPs/TMDs heterostructures, such as the band offsets and interfacial interaction, are of fundamental and technological interest. Here $CsPbBr_3$ and $MoSe_2$ are taken as prototypes of LHPs and 2D TMDs to investigate the band alignment and interfacial coupling between them. Our GGA-PBE and HSE06 calculations reveal an intrinsic type-II band alignment between $CsPbBr_3$ and $MoSe_2$. This type-II band alignment suggests that the performance of $CsPbBr_3$-based photodetectors can be improved by incorporating $MoSe_2$ monolayer. Furthermore, the absence of deep defect states at $CsPbBr_3/MoSe_2$ interfaces is also beneficial to the better performance of photodetectors based on $CsPbBr_3/MoSe_2$ heterostructure. This work not only offers insights into the improved performance of photodetectors based on LHPs/TMDs heterostructures but it also provides guidelines for designing high-efficiency optoelectronic devices based on LHPs/TMDs heterostructures.

Key words: lead halide perovskites; transition metal dichalcogenides; photodetectors; band alignment; interfacial coupling

Citation: L Huang, N J Huo, Z Q Zheng, H F Dong, and J B Li, Two-dimensional transition metal dichalcogenides for lead halide perovskites-based photodetectors: band alignment investigation for the case of $CsPbBr_3/MoSe_2$[J]. *J. Semicond.*, 2020, 41(5), 052206. http://doi.org/10.1088/1674-4926/41/5/052206

1. Introduction

In recent years, lead halide perovskites have attracted enormous attention because of their promising applications in high-performance optoelectronic devices[1–6]. Halide perovskites have high light absorption coefficient, long charge diffusion length, high carrier mobility and high defect tolerance[7–12]. These superior properties make them good candidates for optoelectronic applications, such as solar cells[13–16], photodetectors[17–21] and light-emitting diodes[22, 23], etc. Despite the good performance, halide perovskites potential stability issue remains a major challenge for optoelectronic devices[24–26]. To achieve stable, high-efficiency halide perovskite based optoelectronic devices, other functional layers such as interfacial layers and encapsulation films are required to work together with halide perovskites.

Two-dimensional (2D) materials, such as graphene, transition metal dichalcogenides (TMDs) and black phosphorus, and so on, have excellent electronic, optical, and thermal properties[27–32]. However, atomically thin TMDs hardly absorb light to a sufficient extent for photodetecting and it is necessary to incorporate them with other semiconducting materials such as halide perovskites to improve the performance. To take advantages of the high light absorption of halide perovskites and the excellent carrier transport properties of 2D materials, many 2D materials have been integrated into optoelectronic devices based on halide perovskites to achieve novel electronic and optoelectronic devices with improved performance. For example, by integrating MoS_2 with $CsPbBr_3$ nanosheets, excellent performance has been achieved in the hybrid $MoS_2/CsPbBr_3$-based photodetectors[33]. Cho and co-workers have fabricated hybrid perovskite-graphene photodetector and observed improved performances due to the reduced recombination rates and efficient electron transfer[34]. Integration of MoS_2 with $MAPbI_3$ leads to substantial improvement in the quantum efficiency and the responsivity of the photodetector[35, 36]. Heterostructured $WS_2/MAPbI_3$ is also demonstrated to have an enhanced photoresponse[37].

An exact knowledge of electronic levels is a prerequisite to design optoelectronic devices with good performance and for understanding the device physics[38, 39]. The electronic structures, especially the band alignments, of the hybrid perovskites/TMDs play a key role in the optoelectronic devices. Theoretically, heterostructures with type-II band alignments can facilitate the separation of light-generated electrons and holes. As a result, the carrier recombination can be reduced and their optoelectronic performance can be improved. While for heterostructures with type-I band alignments, both

Correspondence to: H F Dong, hfdong@gdut.edu.cn; J B Li, jbli@semi.ac.cn

Received 29 DECEMBER 2019; Revised 19 FEBRUARY 2020.

electrons and holes tend to concentrate on the same material, which may result in the carrier's reduced lifetime.

A unified understanding of the band offsets in perovskites/TMDs is missing. Even the type of their band alignment (type-I or type-II) is under debate. Furthermore, spin-orbital coupling (SOC) has significant influence on the electronic structures of lead halide perovskites (LHPs) and TMDs[40, 41]. Specifically, for TMDs, significant relativistic effect is observed in their valence band maximum (VBM). In the case of LHPs, very large SOC gaps appear at the conduction band minimum (CBM) in their electronic structures. The role of SOC in the band alignment is far from clear. On the other side, upon two semiconductors making contacts, band bending will occur due to the interfacial interaction. How are the interfacial properties influenced by the interfacial coupling? And, what is the role of SOC in interfacial coupling? These questions are far from being answered and a thorough investigation is required.

In this work, $CsPbBr_3$ and $MoSe_2$ are taken as prototypes of LHPs and 2D TMDs to investigate the band alignment and interfacial coupling between them. Insights into the SOC effects on the band offsets and interfacial coupling are provided. Our GGA-PBE and HSE06 calculations reveal an intrinsic type-II band alignment between $CsPbBr_3$ and $MoSe_2$ with both the VBM and CBM of $MoSe_2$ monolayer being lower in energy than those of $CsPbBr_3$. The conduction band offset is significantly reduced by the large spin-orbital coupling at the CBM of $CsPbBr_3$. Meanwhile, the valence band offset is reduced by Hartree-Fock exchange interaction. Consequently, an intrinsic type-I alignment is achieved. The type-II band alignment recovers upon $CsPbBr_3$ making contacts with $MoSe_2$ due to the interfacial interaction. Furthermore, no deep defect states are observed in the band gap of $CsPbBr_3/MoSe_2$ heterostructures. These results suggest that the performance of $CsPbBr_3$-based photodetectors can be improved by incorporating $MoSe_2$ monolayer.

2. Computational details

We perform our calculations within the projector augmented plane-wave method[42–44] in the VASP code. The exchange correlation functional with partial core correction included is described by using the general gradient approximation (GGA) of Perdew, Burke, and Ernzerhof (PBE)[45, 46]. The plane-wave cutoff energy is set as 450 eV in all the calculations. A vacuum larger than 20 Å along is used to eliminate the interaction between adjacent slabs. All the structures are fully relaxed with a force tolerance of 0.02 eV/Å. HSE06 functional with mixing 25% of screened Hartree-Fock exchange to the GGA-PBE exchange is used to obtain the accurate electronic structures of all of the systems used here[47, 48]. Mixing percentage is adjusted to reproduce the experimental band gaps of $MoSe_2$ monolayer and $CsPbBr_3$ bulk. DFT-D3 method of Grimme[49] is used to correct the van der Waals interaction at $CsPbBr_3/MoSe_2$ interface.

$CsPbBr_3$ in the γ phase, which is proved to be the most stable phase[41], is taken as an example of LHPs and $MoSe_2$ monolayer as a prototype of TMDs to investigate the electronic structures of LHPs/TMDs interfaces. To simulate the interfacial coupling between LHPs and TMDs, a periodic $CsPbBr_3$ slab with a vacuum layer more than 20 Å is constructed here.

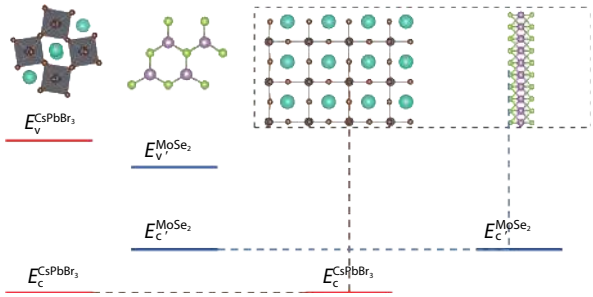

Fig. 1. (Color online) Schematic procedure to calculate the valence band offsets for heterostructured $CsPbBr_3/MoSe_2$. (a) Step I, calculating the energy difference between the VBM and core level in γ-$CsPbBr_3$ and monolayer $MoSe_2$, respectively. (b) Step II, calculating the core levels of each layer in $CsPbBr_3/MoSe_2$ superlattice and doing core-level alignment. A superlattice of $CsPbBr_3/MoSe_2$ is constructed in (b) to do the core-level alignment.

Since γ-$CsPbBr_3$ has a cubic crystal structure. Hence, a rectangle cell of $MoSe_2$ monolayer is constructed to minimize the lattice mismatch between $CsPbBr_3$ and $MoSe_2$ monolayer, as we did in our previous works[50–52]. The $CsPbBr_3/MoSe_2$ interface model contains $1 \times 3 \times 4$ unit cells of α-$CsPbBr_3$ and $1 \times 5 \times 1$ rectangle cells of $MoSe_2$. ($CsPbBr_3$ in α phase is used here because of the limit on computing capability. We have demonstrated that the core levels of Br_1s changed little in α-$CsPbBr_3$ and γ-$CsPbBr_3$. Therefore, using α-$CsPbBr_3$ in the heterostructures here does not influence the validity of our results.) The lattice mismatches along a and b directions are smaller than 4%.

The calculation method for band offsets is illustrated in Fig. 1 and Refs. [53, 54]. Firstly, the energy differences between the core level and the VBM in bulk γ-$CsPbBr_3$ and $MoSe_2$ monolayer are calculated. Then we do the alignment of core levels in $CsPbBr_3/MoSe_2$ heterostructure. The valence band offset, ΔE_v, is calculated as

$$\Delta E_v = \Delta E_{c,v}^{CsPbBr_3} - \Delta E_{c',v'}^{MoSe_2} + \Delta E_{c,c'}, \quad (1)$$

where $\Delta E_{c,v}^{CsPbBr_3}$ is the energy difference between the core level and the VBM of $CsPbBr_3$, $\Delta E_{c',v'}^{MoSe_2}$ is that of $MoSe_2$ monolayer. $\Delta E_{c,c'}$ is the energy difference in core levels of $CsPbBr_3$ and $MoSe_2$ in the $CsPbBr_3/MoSe_2$ heterostructure. The conduction band offset is calculated as

$$\Delta E_c = E_g^{CIS} - E_g^{CdS} + \Delta E_v. \quad (2)$$

Here Br_1s in $CsPbBr_3$ and Se_1s in $MoSe_2$ monolayer are taken as the core levels to do the alignment.

Relativistic first-principles calculations are performed to explore the SOC effect on the electronic structures of $CsPbBr_3$, $MoSe_2$ monolayer and $CsPbBr_3/MoSe_2$ interface and its interfacial coupling. To exclude the impact from other factor on the interfacial coupling, we used the heterostructured $CsPbBr_3/MoSe_2$ structures that optimized by GGA-PBE functional to explore the SOC effects. The interface coupling is characterized by the binding energy, E_b, between $CsPbBr_3$ slab and $MoSe_2$ monolayer, which is calculated as

$$E_b = E_{hetero} - E_{CsPbBr_3} - E_{MoSe_2}, \quad (3)$$

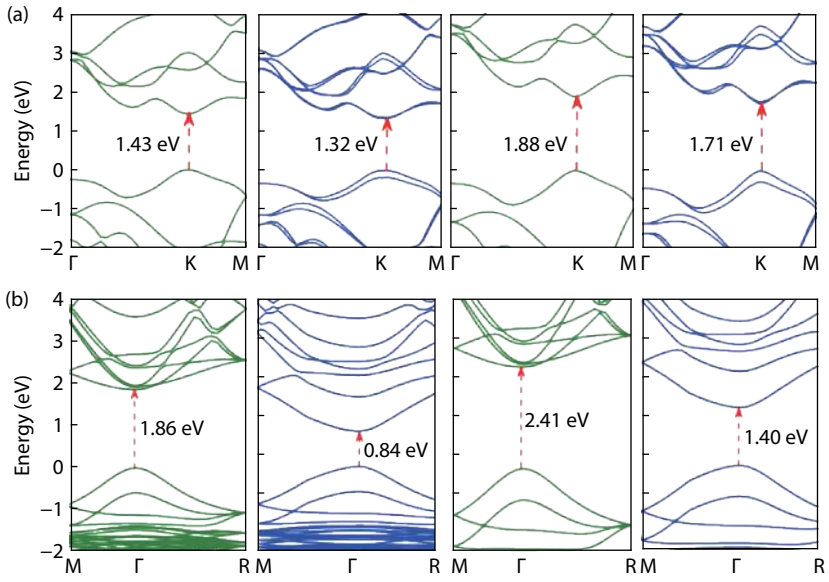

Fig. 2. (Color online) Band structures of (a) γ-$CsPbBr_3$ and (b) $MoSe_2$ monolayer by using PBE (brown lines) and HSE06 (blue lines) functionals. Band structures with and without SOC are both calculated to explore the influence of SOC on the electronic structures. The VBMs are taken as the reference in all the band structures. All of the band gaps are labeled.

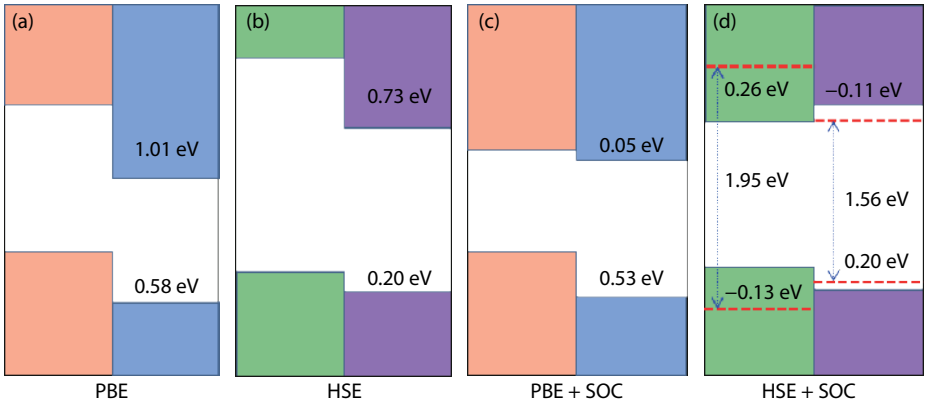

Fig. 3. (Color online) Band alignment of $CsPbBr_3$ and $MoSe_2$ is calculated by using PBE and HSE06 functionals. Conduction and valence band offsets are labeled in black. Red-dashed lines in (d) are the corrected band edges of $CsPbBr_3$ and $MoSe_2$ monolayer with Hatree-Fock exchange percentage of 15% for $MoSe_2$ monolayer and 45% for $CsPbBr_3$. The corrected band gaps are labeled in blue. The conduction and valence band offsets are 0.26 and –0.13 eV, respectively.

where E_{hetero}, E_{MoSe_2} and E_{CsPbBr_3} are the total energies of $CsPbBr_3/MoSe_2$ heterostructure, $MoSe_2$ monolayer and $CsPbBr_3$ slab, respectively.

3. Results and discussion

Fig. 1 shows the crystal structures of γ-$CsPbBr_3$ and monolayer $MoSe_2$, and the schematic alignment procedure to calculate the valence band offsets. The optimized lattice constants of γ-$CsPbBr_3$ are $a = b = 8.33$ Å, $c = 11.91$ Å. The lattice constants of monolayer $MoSe_2$ are $a = b = 3.33$ Å. To do the alignment of the core levels, a superlattice of α-$CsPbBr_3/MoSe_2$ is constructed (Fig. 1(b)). During the core level alignment calculations, the lattice constants of α-$CsPbBr_3$ are fixed and strains are applied to the monolayer $MoSe_2$.

At the first step of band offset calculation (Fig. 1(a)), we calculated the electronic structures of γ-$CsPbBr_3$ and $MoSe_2$ monolayer in Fig. 2. $MoSe_2$ monolayer shows a direct band gap of 1.43 eV by GGA-PBE functional and 1.88 eV by HSE06 functional. It has been demonstrated that SOC have significant influence on the VBM at K point in the electronic structures of TMDs. The calculated SOC gap here is 0.18 eV by GGA-PBE functional and 0.28 eV by HSE06 functional. These results agree well with previous works[55]. In Fig. 2(b), the band structures of γ-$CsPbBr_3$ are calculated by PBE, PBE + SOC, HSE06 and HSE06 + SOC methods. γ-$CsPbBr_3$ shows a direct band gap at the Γ point regardless of the functionals. Previous works have demonstrated that the VBMs of LHPs are formed by an antibonding of Pb_s and p orbitals of halides. Their CBMs are dominated by Pb_6p orbitals. Due to the large relativistic effect of Pb_6p orbitals, the LHPs always exhibit an extremely large SOC gap at the CBMs. The band structures of γ-$CsPbBr_3$ in Fig. 2(b) show that an SOC splitting about 1 eV appears at the CBM. After including SOC, the band gap of γ-$CsPbBr_3$ is significantly reduced. The large SOC of γ-$CsPbBr_3$ may have significant influence on the band alignments of heterostructured γ-$CsPbBr_3$/TMDs.

In photodetectors based on LHPs/TMDs heterostructures, the band offsets at the interfaces play an important role in

their optoelectronic performance. In Figs. 3(a) and 3(b), the band alignment of $CsPbBr_3/MoSe_2$ is calculated by using PBE and HSE06 functionals. A type-II band alignment is found for both functionals. Specifically, both the VBM and CBM of $MoSe_2$ are lower than those of $CsPbBr_3$, suggesting that electrons and holes will separate spontaneously with electrons concentrating in $MoSe_2$ layer and holes concentrating in $CsPbBr_3$. Therefore, in optoelectronic devices based on $CsPbBr_3/MoSe_2$, the recombination will be reduced and the efficiency can be improved. Comparing the results in Figs. 3(a) and 3(b), larger band gaps are obtained by HSE06 functional than PBE functional. It is found that HSE06 calculation obtains reduced conduction and valence band offsets than PBE results. It should be noted that PBE calculation underestimates the band gaps of $CsPbBr_3$ and monolayer $MoSe_2$ than their experimental values.

It has been demonstrated in Fig. 2 that SOC has a significant influence on the band edges of $CsPbBr_3$ and $MoSe_2$ monolayer. Consequently, the band offsets between $CsPbBr_3$ and $MoSe_2$ monolayer can be changed accordingly. When SOC effect included, as shown in Figs. 3(c) and 3(d), our results indicate that the CBM of $CsPbBr_3$ shifts down because of the SOC splitting, resulting in a reduced band gap. Furthermore, the conduction band offset, ΔE_c, is much reduced due to the large SOC splitting at the CBM of $CsPbBr_3$. On the other hand, the influence of SOC on the valence band offset, ΔE_v, is rather weak. Additionally, HSE + SOC calculations indicate a type-I band alignment of $CsPbBr_3/MoSe_2$ with band edges of $CsPbBr_3$ encapsulated in that of $MoSe_2$ monolayer. This divergence with experimental results may result from their uncorrected band edges. To reproduce the experimental band gaps of $CsPbBr_3$ and $MoSe_2$ monolayer, we calculated their electronic structures by changing the mixing percentages of Hartree-Fock exchange (15% for $MoSe_2$ monolayer and 45% for $CsPbBr_3$) into the GGA-PBE exchange functional. Then, the $MoSe_2$ monolayer and 45% for $CsPbBr_3$ show corrected band gaps of 1.56 and 1.95 eV, respectively, which are in good consist with experimental values. The corrected band alignment is shown by the dashed lines in Fig. 3(d). Type-I band alignment of $CsPbBr_3/MoSe_2$ is maintained after corrections. What makes difference is that the VBM of $CsPbBr_3$ shifts downward to below that of $MoSe_2$ and its CBM shifts upward to higher than that of $MoSe_2$. In this case, both the photon-generated electrons and holes tend to concentrate in the $MoSe_2$ layer. As a result, the performance of photodetectors based on $CsPbBr_3/MoSe_2$ can be limited by the electron-hole recombination in $MoSe_2$ layer.

It has been demonstrated that the band offsets of a heterostructure can be modulated by interfacial interaction. In Fig. 4, we explored the interfacial interaction between $MoSe_2$ layer and $CsPbBr_3$ slabs with CsBr and PbBr terminated. Our results show that $MoSe_2$ layer exhibits a stronger binding to PbBr-terminated $CsPbBr_3$ slab ($E_b = -1.907$ eV per supercell) than to CsBr-terminated one (−1.699 eV). Additionally, SOC effect is revealed to have little influence on the interfacial coupling. (The binding energies become −1.900 and −1.701 eV for corresponding systems above when SOC effect included.) The results of charge difference in Fig. 4 suggest that charge transfer occurs at the $CsPbBr_3/MoSe_2$ interface. For both cases, a little negative charge (electrons) transfers

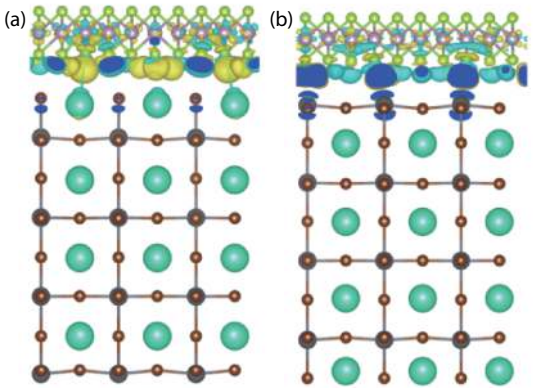

Fig. 4. (Color online) The charge difference at the interfaces between $MoSe_2$ monolayer and (a) CsBr-terminated, (b) PbBr-terminated $CsPbBr_3$ slab.

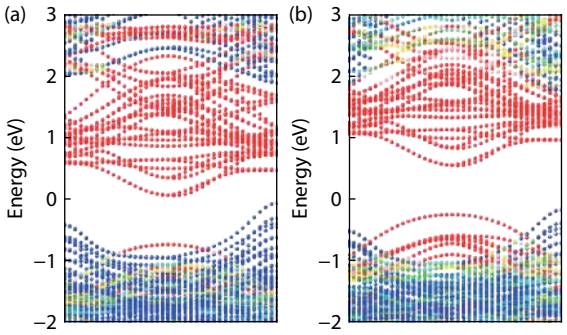

Fig. 5. (Color online) The projected band structures of $CsPbBr_3/MoSe_2$ heterostructures. (a) Interface between $MoSe_2$ and CsBr-terminated $CsPbBr_3$. (b) Interface between $MoSe_2$ and PbBr-terminated $CsPbBr_3$. The red and blue dots represent the bands dominated by $MoSe_2$ layer and $CsPbBr_3$, respectively.

from the interfacial metal atoms of $CsPbBr_3$ slab to Se atoms of $MoSe_2$ layer, suggesting a higher CBM of $CsPbBr_3$ slab than $MoSe_2$ monolayer.

It is known that interfacial charge transfer has influence on the band offsets at interfaces. In Fig. 5, the projected band structures of $CsPbBr_3/MoSe_2$ interfaces are calculated to check their band alignments. The bands dominated by $CsPbBr_3$ and $MoSe_2$ are plotted by blue and red dots in Fig. 5. Our results indicate type-II band alignment in both $CsPbBr_3/MoSe_2$ interfaces with the CBM and VBM of $CsPbBr_3$ higher than those of $MoSe_2$ layer. Furthermore, there is no deep defect states appear in the band gaps of $CsPbBr_3/MoSe_2$ heterostructures, suggesting rather low density of non-radiative recombination center at the interface. This is attributed to the high defect tolerance of $CsPbBr_3$ and no dangling bonds of $MoSe_2$ layer. So, the performance of $CsPbBr_3$ based photodetectors can be improved by inserting a $MoSe_2$ layer to facilitate the separation of photo-generated electrons and holes.

It has been demonstrated that if we change the halide atom from Br to I, better light absorption usually can be obtained thanks to reduced band gaps that arise because of the CBM and the VBM approaches the Fermi level[54]. Additionally, the VBM of MoS_2 monolayer is lower than that of $MoSe_2$ monolayer. Consequently, the downshift of the VBM of $CsPbI_3$ and the upshift of the VBM of MoS_2 will lead to a type-II band alignment in $CsPbI_3/MoS_2$, with a larger valence band offset than that in $CsPbBr_3/MoSe_2$. In this view, better perfor-

mance can be obtained in photodetectors based on $CsPbI_3$/MoS_2 than those based on $CsPbBr_3$/$MoSe_2$. Our results in this work provide guidelines for designing high-performance optoelectronic devices based on hybrid LHPs and TMDs.

4. Conclusion

In summary, $CsPbBr_3$ and $MoSe_2$ are taken as prototypes of LHPs and 2D TMDs to investigate the band alignment between them. A type-II band alignment between $CsPbBr_3$ and $MoSe_2$ is manifested by our first-principles calculations by using GGA-PBE and HSE06 functionals. Both the VBM and CBM of $MoSe_2$ monolayer are lower in energy than those of $CsPbBr_3$. The conduction band offset is significantly reduced by the large spin-orbital coupling at the CBM of $CsPbBr_3$, resulting in an intrinsic type-I alignment between them by careful HSE06 + SOC calculations. Upon $CsPbBr_3$ making contacts with $MoSe_2$, the interfacial interaction leads to the upshift of the bands of $CsPbBr_3$ and downshift of the bands of $MoSe_2$, further resulting a type-II band alignment between them. This type-II band alignment suggests that the performance of $CsPbBr_3$-based photodetectors can be improved by incorporating $MoSe_2$ monolayer. Furthermore, the absence of deep defect states at $CsPbBr_3$/$MoSe_2$ interfaces is also beneficial to the better performance of photodetectors based on $CsPbBr_3$/$MoSe_2$ heterostructure. This work not only uncovers the mechanism of improved performance of photodetectors based on $CsPbBr_3$/$MoSe_2$ heterostructures but it also provide guidelines for designing high-efficiency optoelectronic devices based on LHPs/TMDs heterostructures.

Acknowledgements

This work was financially supported by the National Natural Science Foundation of China (Grants No. 11804058, 11674310, 61622406).

References

[1] Zhang W, Eperon G E, Snaith H J. Metal halide perovskites for energy applications. Nat Energy, 2016, 1, 16048
[2] Stoumpos C C, Kanatzidis M G. Halide perovskites: poor man's high-performance semiconductors. Adv Mater, 2016, 28, 5778
[3] Lin Q, Armin A, Burn P L, et al. Organohalide perovskites for solar energy conversion. Acc Chem Res, 2016, 49, 545
[4] Zhao Y, Zhu K. Organic–inorganic hybrid lead halide perovskites for optoelectronic and electronic applications. Chem Soc Rev, 2016, 45, 655
[5] Chen J, Zhou S, Jin S, et al. Crystal organometal halide perovskites with promising optoelectronic applications. J Mater Chem C, 2016, 4, 11
[6] Berry J, Buonassisi T, Egger D A, et al. Hybrid organic–inorganic perovskites (HOIPs): Opportunities and challenges. Adv Mater, 2015, 27, 5102
[7] Lee M M, Teuscher J, Miyasaka T, et al. Efficient hybrid solar cells based on meso-superstructured organometal halide perovskites. Science, 2012, 338, 643
[8] Stranks S D, Eperon G E, Grancini G, et al. Electron-hole diffusion lengths exceeding 1 micrometer in an organometal trihalide perovskite absorber. Science, 2013, 342, 341
[9] Liu D, Kelly T L. The emergence of perovskite solar cells. Nat Photonics, 2014, 8, 133
[10] Jang D M, Park K, Kim D H, et al. Reversible halide exchange reaction of organometal trihalide perovskite colloidal nanocrystals for full-range band gap tuning. Nano Lett, 2015, 15, 5191
[11] Dong R, Fang Y, Chae J, et al. High-gain and low-driving-voltage photodetectors based on organolead triiodide perovskites. Adv Mater, 2015, 27, 1912
[12] Veldhuis S A, Boix P P, Yantara N, et al. Perovskite materials for light-emitting diodes and lasers. Adv Mater, 2016, 28, 6804
[13] Liu M, Johnston M B, Snaith H J. Efficient planar heterojunction perovskite solar cells by vapour deposition. Nature, 2013, 501, 395
[14] Zhou H, Chen Q, Li G, et al. Interface engineering of highly efficient perovskite solar cells. Science, 2014, 345, 542
[15] Mei A, Li X, Liu L, et al. A hole-conductor–free, fully printable mesoscopic perovskite solar cell with high stability. Science, 2014, 345, 295
[16] Zuo C, Bolink H J, Han H, et al. Advances in perovskite solar cells. Adv Sci, 2016, 3, 1500324
[17] Lin Q, Armin A, Burn P L, et al. Filterless narrowband visible photodetectors. Nat Photonics, 2015, 9, 687
[18] Fang Y, Dong Q, Shao Y, et al. Highly narrowband perovskite single-crystal photodetectors enabled by surface-charge recombination. Nat Photonics, 2015, 9, 679
[19] Chen S, Teng C, Zhang M, et al. A flexible UV-Vis-NIR photodetector based on a perovskite/conjugated-polymer composite. Adv Mater, 2016, 28, 5969
[20] Zhu H L, Cheng J, Zhang D, et al. Room-temperature solution-processed niox: PbI_2 nanocomposite structures for realizing high-performance perovskite photodetectors. ACS Nano, 2016, 10, 6808
[21] Tan Z K, Moghaddam R S, Lai M L, et al. Bright light-emitting diodes based on organometal halide perovskite. Nat Nanotechnol, 2014, 9, 687
[22] Cho H, Jeong S H, Park M H, et al. Overcoming the electroluminescence efficiency limitations of perovskite light-emitting diodes. Science, 2015, 350, 1222
[23] Stranks S D, Snaith H J. Metal-halide perovskites for photovoltaic and light-emitting devices. Nat Nanotechnol, 2015, 10, 391
[24] Yang J, Siempelkamp B D, Liu D, et al. Investigation of $CH_3NH_3PbI_3$ degradation rates and mechanisms in controlled humidity environments using in situ techniques. ACS Nano, 2015, 9, 1955
[25] Hailegnaw B, Kirmayer S, Edri E, et al. Rain on methylammonium lead iodide based perovskites: possible environmental effects of perovskite solar cells. J Phys Chem Lett, 2015, 6, 1543
[26] Zhang Y Y, Chen S, Xu P, et al. Intrinsic instability of the hybrid halide perovskite semiconductor $CH_3NH_3PbI_3$. Chin Phys Lett, 2018, 35, 036104
[27] Novoselov K S, Geim A K, Morozov S V, et al. Two-dimensional gas of massless Dirac fermions in graphene. Nature, 2005, 438, 197
[28] Lee C, Wei X, Kysar J W, et al. Measurement of the elastic properties and intrinsic strength of monolayer graphene. Science, 2008, 321, 385
[29] Bonaccorso F, Sun Z, Hasan T, et al. Graphene photonics and optoelectronics. Nat Photonics, 2010, 4, 611
[30] Sun Y, Wu Q, Shi G. Graphene based new energy materials. Energy Environ Sci, 2011, 4, 1113
[31] Li Y, Xu L, Liu H, et al. Graphdiyne and graphyne: from theoretical predictions to practical construction. Chem Soc Rev, 2014, 43, 2572
[32] Bonaccorso F, Colombo L, Yu G, et al. Graphene, related two-dimensional crystals, and hybrid systems for energy conversion and storage. Science, 2015, 347, 1246501
[33] Song X, Liu X, Yu D, et al. Boosting two-dimensional MoS_2/$CsPbBr_3$ photodetectors via enhanced light absorbance and interfacial carrier separation. ACS Appl Mater Interfaces, 2018, 10, 2801
[34] Lee Y, Kwon J, Hwang E, et al. High-performance perovskite-graphene hybrid photodetector. Adv Mater, 2015, 27, 41
[35] Wang Y, Fullon R, Acerce M, et al. Solution-processed MoS_2/organolead trihalide perovskite photodetectors. Adv Mater, 2017, 29, 1603995

[36] Kang D H, Pae S R, Shim J, et al. An ultrahigh-performance photodetector based on a perovskite-transition-metal-dichalcogenide hybrid structure. Adv Mater, 2016, 28, 7799
[37] Ma C, Shi Y, Hu W, et al. Heterostructured $WS_2/CH_3NH_3PbI_3$ photoconductors with suppressed dark current and enhanced photodetectivity. Adv Mater, 2016, 28, 3683
[38] Schulz P, Edri E, Kirmayer S, et al. Interface energetics in organo-metal halide perovskite-based photovoltaic cells. Energy Environ Sci, 2014, 7, 1377
[39] Kabra D, Lu L P, Song M H, et al. Efficient single-layer polymer light-emitting diodes. Adv Mater, 2010, 22, 3194
[40] Kormányos A, Zólyomi V, Drummond N D, et al. Spin-orbit coupling, quantum dots, and qubits in monolayer transition metal dichalcogenides. Phys Rev X, 2014, 4, 011034
[41] Yin W J, Yang J H, Kang J, et al. Halide perovskite materials for solar cells: a theoretical review. J Mater Chem A, 2015, 3, 8926
[42] Blöchl P E. Projector augmented-wave method. Phys Rev B, 1994, 50, 17953
[43] Kresse G, Joubert D. From ultrasoft pseudopotentials to the projector augmented-wave method. Phys Rev B, 1991, 59, 1758
[44] Kresse G, Furthmüller J. Efficiency of ab-initio total energy calculations for metals and semiconductors using a plane-wave basis set. Comput Mater Sci, 1996, 6, 15
[45] Perdew J P, Wang Y. Density-functional approximation for the correlation energy of the inhomogeneous electron gas. Phys Rev B, 1986, 33, 8800
[46] Perdew J P, Burke K, Ernzerhof M. Generalized gradient approximation made simple. Phys Rev Lett, 1996, 77, 3865
[47] Heyd J, Peralta J E, Scuseria G E, et al. Energy band gaps and lattice parameters evaluated with the Heyd-Scuseria-Ernzerhof screened hybrid functional. J Chem Phys, 2005, 123, 174101
[48] Heyd J, Scuseria G E, Ernzerhof M. Hybrid functionals based on a screened Coulomb potential. J Chem Phys, 2006, 124, 9906
[49] Grimme S, Antony J, Ehrlich S, et al. A consistent and accurate ab initio parametrization of density functional dispersion correction (DFT-D) for the 94 elements H-Pu. J Chem Phys, 2010, 132, 154104
[50] Huang L, Huo N, Li Y, et al. Electric-field tunable band offsets in black phosphorus and MoS_2 van der Waals pn heterostructure. J Phys Chem Lett, 2015, 6, 2483
[51] Huang L, Tao L, Gong K, et al. Role of defects in enhanced Fermi level pinning at interfaces between metals and transition metal dichalcogenides. Phys Rev B, 2017, 96, 205303
[52] Huang L, Zhong M, Deng H X, et al. The Coulomb interaction in van der Waals heterostructures. Sci China: Phys Mech Astron, 2019, 62(3), 37311
[53] Wei S H, Zunger A. Band offsets and optical bowings of chalcopyrites and Zn-based II–VI alloys. J Appl Phy, 1995, 78, 3846
[54] Butler K T, Frost J M, Walsh A. Band alignment of the hybrid halide perovskites $CH_3NH_3PbCl_3$, $CH_3NH_3PbBr_3$ and $CH_3NH_3PbI_3$. Mater Horizons, 2015, 2, 228
[55] Zhu Z Y, Cheng Y C, Schwingenschlögl U. Giant spin-orbit-induced spin splitting in two-dimensional transition-metal dichalcogenide semiconductors. Phys Rev B, 2011, 84, 153402